Title

Engineering three-dimensional hybrid supercapacitors and microsupercapacitors for high-performance integrated energy storage

Journal

Proceedings of the National Academy of Sciences of the United States of America, 112(14)

ISSN

0027-8424

Authors

El-Kady, Maher F
Ihns, Melanie
Li, Mengping
et al.

Publication Date

2015-04-07

DOI

10.1073/pnas.1420398112

Peer reviewed

Engineering three-dimensional hybrid supercapacitors and microsupercapacitors for high-performance integrated energy storage

Maher F. El-Kady[a,b], Melanie Ihns[a], Mengping Li[a], Jee Youn Hwang[a], Mir F. Mousavi[a,c], Lindsay Chaney[a], Andrew T. Lech[a], and Richard B. Kaner[a,d,1]

[a]Department of Chemistry and Biochemistry and California NanoSystems Institute, University of California, Los Angeles, CA 90095; [b]Department of Chemistry, Faculty of Science, Cairo University, Giza 12613, Egypt; [c]Department of Chemistry, Tarbiat Modares University, Tehran 14115-175, Iran; and [d]Department of Materials Science and Engineering, University of California, Los Angeles, CA 90095

Edited by Alexis T. Bell, University of California, Berkeley, CA, and approved March 4, 2015 (received for review October 30, 2014)

Supercapacitors now play an important role in the progress of hybrid and electric vehicles, consumer electronics, and military and space applications. There is a growing demand in developing hybrid supercapacitor systems to overcome the energy density limitations of the current generation of carbon-based supercapacitors. Here, we demonstrate 3D high-performance hybrid supercapacitors and microsupercapacitors based on graphene and MnO_2 by rationally designing the electrode microstructure and combining active materials with electrolytes that operate at high voltages. This results in hybrid electrodes with ultrahigh volumetric capacitance of over 1,100 F/cm^3. This corresponds to a specific capacitance of the constituent MnO_2 of 1,145 F/g, which is close to the theoretical value of 1,380 F/g. The energy density of the full device varies between 22 and 42 Wh/l depending on the device configuration, which is superior to those of commercially available double-layer supercapacitors, pseudocapacitors, lithium-ion capacitors, and hybrid supercapacitors tested under the same conditions and is comparable to that of lead acid batteries. These hybrid supercapacitors use aqueous electrolytes and are assembled in air without the need for expensive "dry rooms" required for building today's supercapacitors. Furthermore, we demonstrate a simple technique for the fabrication of supercapacitor arrays for high-voltage applications. These arrays can be integrated with solar cells for efficient energy harvesting and storage systems.

supercapacitor | microsupercapacitor | graphene | metal oxide

As a result of the rapidly growing energy needs of modern life, the development of high-performance energy storage devices has gained significant attention. Supercapacitors are promising energy storage devices with properties intermediate between those of batteries and traditional capacitors, but they are being improved more rapidly than either (1). Over the past couple of decades, supercapacitors have become key components of everyday products by replacing batteries and capacitors in an increasing number of applications. Their high power density and excellent low-temperature performance have made them the technology of choice for backup power, cold starting, flash cameras, regenerative braking, and hybrid electric vehicles (2, 3). The future growth of this technology depends on further improvements in energy density, power density, calendar and cycle life, and production cost.

According to their charge storage mechanism, supercapacitors are classified as either electric double-layer capacitors (EDLCs) or pseudocapacitors (2). In EDLCs, charge is stored through rapid adsorption–desorption of electrolyte ions on high-surface-area carbon materials, whereas pseudocapacitors store charge via fast and reversible Faradaic reactions near the surface of metal oxides or conducting polymers. The majority of supercapacitors currently available in the market are symmetric EDLCs featuring activated carbon electrodes and organic electrolytes that provide cell voltages as high as 2.7 V. Although these EDLCs exhibit high power density and excellent cycle life, they suffer from low energy density because of the limited capacitance of carbon-based electrodes. The specific pseudocapacitance of Faradaic electrodes (typically 300–1,000 F/g) exceeds that of carbon-based EDLCs; however, their performance tends to degrade quickly upon cycling.

Studies during the past few years have demonstrated an attractive alternative to conventional EDLCs and pseudocapacitors by using hybrid systems. Using both Faradaic and non-Faradaic processes to store charge, hybrid capacitors can achieve energy and power densities greater than EDLCs without sacrificing the cycling stability and affordability that have so far limited the success of pseudocapacitors (4). Several combinations of materials, such as RuO_2 (5), Co_3O_4 (6), NiO (7), V_2O_5 (8), $Ni(OH)_2$ (9), and MnO_2 (10), have been studied for preparing hybrid supercapacitors. Among these, MnO_2-based systems are particularly attractive as MnO_2 is an earth-abundant and environmentally friendly material with a high theoretical specific capacitance of 1,380 F/g (11). However, the poor ionic (10^{-13} S/cm) and electronic (10^{-5}–10^{-6} S/cm) conductivity of pristine MnO_2 often limits its electrochemical performance. Recent reports show that some high-performance results can be achieved only from ultrathin MnO_2 films that are a few tens of nanometers in thickness (12). Nevertheless, the thickness and the area-normalized capacitance of these electrodes are not adequate for most applications. A promising approach to realize practical applications of MnO_2 is to incorporate nanostructured MnO_2 on highly conductive support materials with high surface areas such as nickel nanocones (13), Mn nanotubes (14), activated carbon (15), carbon fabric (16), conducting polymers (17), carbon nanotubes (18, 19), and graphene (20–24). Although promising

Significance

Batteries run just about everything portable in our lives such as smartphones, tablets, computers, etc. Although we have become accustomed to the rapid improvement of portable electronics, the slow development of batteries is holding back technological progress. Thus, it is imperative to develop new energy storage devices that are compact, reliable, and energy dense, charge quickly, and possess both long cycle life and calendar life. Here, we developed hybrid supercapacitors that can store as much charge as a lead acid battery, yet they can be recharged in seconds compared with hours for conventional batteries.

Author contributions: M.F.E.-K. designed research; M.F.E.-K., M.I., M.L., J.Y.H., and L.C. performed research; A.T.L. contributed new reagents/analytic tools; M.F.E.-K., M.I., M.L., J.Y.H., M.F.M., and R.B.K. analyzed data; and M.F.E.-K. wrote the paper.

Conflict of interest statement: This work was supported by Nanotech Energy, Inc.

This article is a PNAS Direct Submission.

[1]To whom correspondence should be addressed. Email: kaner@chem.ucla.edu.

This article contains supporting information online at www.pnas.org/lookup/suppl/doi:10.1073/pnas.1420398112/-/DCSupplemental.

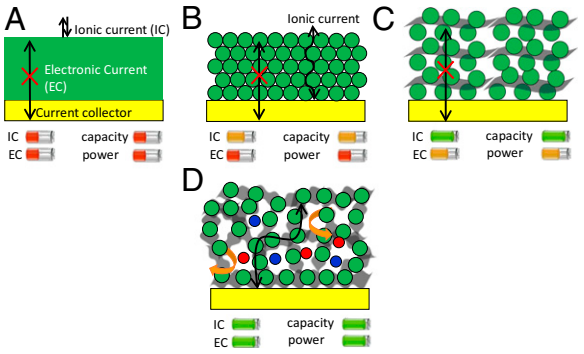

Fig. 1. Rational design of high-energy–high-power hybrid supercapacitor electrodes. Improving the ionic current (IC) and electronic current (EC) within the electrode is a key. Different approaches have been explored including (*A*) compact thick films of metal oxide (here, MnO_2); (*B*) nanostructured metal oxide films; (*C*) addition of conductive materials to the nanostructured metal oxide; and (*D*) our approach is growing nanostructured metal oxide on 3D interconnected graphene networks with high surface area and high electronic conductivity.

specific capacitances of 148–410 F/g have been achieved, such values were obtained only under slow charge–discharge rates and they were found to decrease rapidly as the discharge rate was increased. Moreover, many of these materials have low packing density with large pore volume, meaning that a huge amount of electrolyte is needed to build the device, which adds to the mass of the device without adding any capacitance (25). Accordingly, the energy density and power density of these systems are very limited on the device level. To solve these critical problems, we have developed promising hybrid electrodes based on 3D graphene doped with MnO_2 nanoflowers. By rationally designing the structure of the graphene substrate to achieve high conductivity, suitable porosity, and high specific surface area, one may expect to not only achieve a high gravimetric capacitance, but also to improve the volumetric capacitance (23). Furthermore, the high surface area of nanostructured MnO_2 provides more active sites for the Faradaic reactions and shortens the ion diffusion pathways that are crucial for realizing its full pseudocapacitance. We show that hybrid supercapacitors based on these materials can achieve energy densities of up to 42 Wh/l compared with 7 Wh/l for state-of-the-art commercially available carbon-based supercapacitors. Interestingly, these graphene–MnO_2 hybrid supercapacitors use aqueous electrolytes and are assembled in air without the need for the expensive dry rooms required for building today's supercapacitors.

Whereas great efforts have been made for the fabrication of macroscale hybrid supercapacitors, there are only a few studies on the design and integration of hybrid materials into microsupercapacitors (26). This is likely due to complicated microfabrication techniques that often involve building 3D microelectrodes with micrometer separations. Here, we present a simple, yet versatile technique for the fabrication of 3D hybrid microsupercapacitors based on graphene and MnO_2. These microdevices enable an ultrahigh capacitance per footprint approaching 400 mF/cm^2, which is among the highest values achieved for any microsupercapacitor (26). They can also provide an energy density of up to 22 Wh/l, more than two times that of lithium thin-film batteries. These developments are promising for microelectronic devices such as biomedical sensors and radiofrequency identification tags where high capacity per footprint is crucial.

Results

In designing supercapacitor electrodes, special efforts are made to ensure that they are capable of providing high energy density and high power density. This requires optimization of the preparation conditions to facilitate ionic and electronic transport within the electrodes (27) as illustrated in Fig. 1 (see also *SI Appendix*, section 1).

Synthesis and Characterization of 3D Macroporous Laser-Scribed-Graphene–MnO_2 Electrodes. To experimentally realize energy-dense and high-power supercapacitor electrodes, we integrated a highly conductive and high-surface-area 3D laser-scribed graphene (LSG) framework with MnO_2 as schematically illustrated in Fig. 2*A*. The 3D LSG framework was produced from the laser scribing of GO films following our previously reported method (27), upon which the color changes from golden brown to black. The LSG framework was subsequently coated in situ with MnO_2 using an electrochemical deposition technique as described in *Materials and Methods*; Fig. 2*B*. Note in Fig. 2*B* that the graphene electrode turns darker in color after electrodeposition, a visual indication of the loading of MnO_2. It is well accepted that the conductivity and mass loading of the active materials have a significant impact on the electrochemical behavior of supercapacitor electrodes. Here, the mass loading of MnO_2 is controlled by adjusting the deposition current and deposition time. Fig. 2*C* shows that the MnO_2 loading changes almost linearly with the deposition time at an applied current of 0.25 mA/cm^2 and an average deposition rate estimated to be ~6 μg/min.

In addition to interesting electrical properties, the LSG–MnO_2 electrodes are monolithic and demonstrate superb mechanical integrity under large mechanical deformation. Fig. 2*D* shows that an LSG–MnO_2 electrode can be bent significantly without damage. We evaluated the foldability of LSG–MnO_2 electrodes by measuring their electrical resistance under successive bending cycles. The resistance varies only slightly up to a bending radius of 5.0 mm and can be completely recovered after straightening no matter whether the bending is positive (convex) or negative (concave). Notably, after 1,000 cycles of bending and straightening at a concave bend radius of 5.0 mm, the resistance has increased by only about 2.8%; Fig. 2*E*.

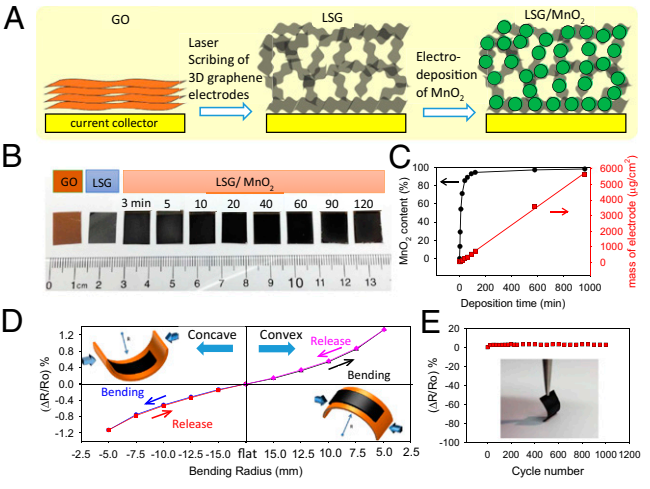

Fig. 2. Fabrication and characterization of LSG/MnO_2 electrodes. (*A*) Schematic diagram presents the fabrication procedure for the LSG–MnO_2 electrodes. (*B*) Digital photographs show a GO film before and after laser scribing. The LSG is then loaded with MnO_2, whose amount can be controlled by adjusting the deposition time from 3 to 120 min. (*C*) Mass loading of MnO_2 versus deposition time. (*D*) Variation of the resistance of an LSG–MnO_2 electrode as a function of bending radius. (*E*) Resistance change of an LSG–MnO_2 electrode under repeated bending cycles for a concave bend radius of 5 mm. (*Inset*) Photograph showing the flexibility of an LSG–MnO_2 electrode.

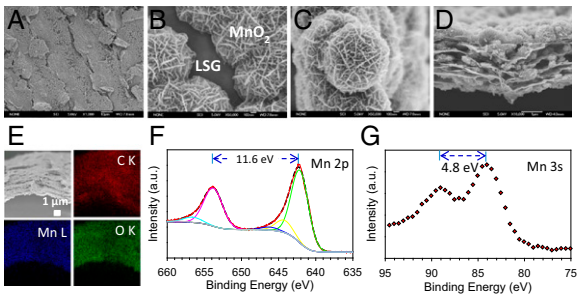

Fig. 3. Morphological and structural characterization of LSG–MnO_2 electrodes. (*A* and *B*) SEM images of an LSG–MnO_2 electrode at low and high magnification. (*C*) SEM image shows the nanoflower morphology of electrodeposited MnO_2. (*D*) Cross-sectional SEM image of an LSG–MnO_2. (*E*) EDS elemental mapping of C (red), Mn (blue), and O (green). (*F*) XPS spectra of Mn 2p showing a doublet with a peak-to-peak separation of 11.6 eV. (*G*) XPS spectra of Mn 3s.

The evolution of morphology corresponding to different deposition times was examined by scanning electron microscopy (SEM); Fig. 3 *A*–*D*. The SEM micrographs show the general morphology and detailed microstructure of a typical sample prepared by 120 min of deposition. MnO_2 has been uniformly coated onto the surface of graphene throughout the entire film. Moreover, the electrodeposited MnO_2 particles show a nanoflower-shaped hierarchical architecture with a clear interface between MnO_2 and the graphene substrate which is consistent with previous studies (20). Closer inspection of the MnO_2 nanoflowers shows that they are made up of hundreds of ultrathin nanoflakes that are 10–20 nm thick (see also *SI Appendix*, Fig. S3). These nanoflakes are interconnected together to form mesoporous MnO_2 with a large accessible surface area, thus offering numerous electroactive sites available to the electrolyte which promotes fast surface Faradaic reactions.

The 3D structure of LSG–MnO_2 electrodes was further analyzed using cross-sectional SEM; Fig. 3*D*. The 3D porous structure of LSG is preserved after the deposition of MnO_2 without any agglomerations. The graphene surface has been uniformly coated with MnO_2 over the entire cross-section. In addition, energy-dispersive X-ray spectroscopy (EDS) provides elemental maps of C, O, and Mn, which confirms that a homogeneous coating of MnO_2 throughout the 3D macroporous framework has been created. The X-ray photoelectron spectroscopy (XPS) data shown in Fig. 3 *F* and *G* further confirm the chemical composition of the deposited oxide; see *SI Appendix* for details.

Assembly and Electrochemical Performance of Symmetric LSG–MnO_2 Supercapacitors. To test the electrochemical performance of LSG–MnO_2 macroporous frameworks, a supercapacitor pouch cell was assembled from two symmetric electrodes separated by a Celgard M824 ion porous separator and impregnated with 1.0 M Na_2SO_4 electrolyte; Fig. 4*A*. The cells were tested by cyclic voltammetry (CV) over a wide range of scan rates from 1 to 1,000 mV/s. As an example, consider the LSG–MnO_2 sample with a deposition time of 3 min: the supercapacitor shows nearly rectangular CV profiles up to a scan rate as high as 1,000 mV/s, indicating excellent charge storage characteristics and ultrafast response time for the electrodes; Fig. 4*B*. The capacitances of the devices made with different deposition times were calculated from CV profiles and are presented in Fig. 4*C*. Note that the capacitance was calculated using the total volume of the cell stack, rather than a single electrode. This includes the volume of the current collector, the active material, the separator, and the electrolyte.

We observe that the capacitance depends strongly on the loading amount of the pseudocapacitive MnO_2 and increases significantly with deposition time from 0 to 960 min. For example, a stack capacitance of up to ~203 F/cm^3 can be achieved with the sample at a 960-min deposition time. This translates to a volumetric capacitance of 1,136.5 F/cm^3 when calculated based on the volume of the active material per electrode only. This value is much higher than the capacitance of activated carbons (60–80 F/cm^3), carbide-derived carbons (180 F/cm^3), bare LSG (12 F/cm^3), activated microwave exfoliated graphite oxide (60 F/cm^3), and liquid-mediated chemically converted graphene (CCG) films (263.3 F/cm^3), indicating that the volumetric capacitance of carbon-based electrodes can be significantly improved by incorporating pseudocapacitive materials (*SI Appendix*, Table S1). Furthermore, this value is higher than some of the best values reported previously for MnO_2-based supercapacitors: 16.1 F/cm^3 for carbon nanotube-polypyrrole–MnO_2 sponge, 130 F/cm^3 for graphene–MnO_2–CNT, 246 F/cm^3 for CNT–MnO_2, 108 F/cm^3 for

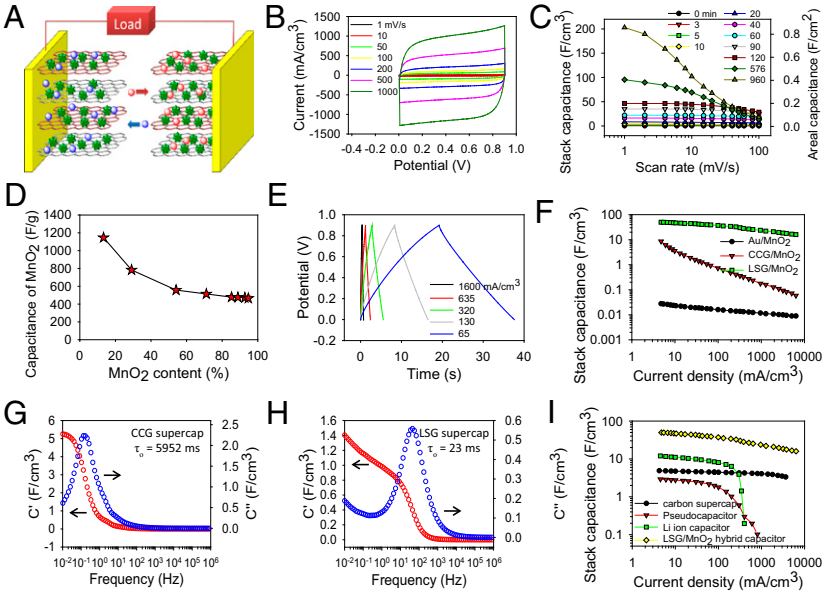

Fig. 4. Electrochemical performance of LSG–MnO_2 symmetric supercapacitors. (*A*) Schematic of the device. (*B*) CV profiles for an LSG–MnO_2 (3 min) supercapacitor at different scan rates. (*C*) Evolution of the stack capacitance of LSG with various mass loadings of MnO_2 as a function of scan rate. (*D*) Specific capacitance due to MnO_2 only as a function of the loadings measured at a scan rate of 1 mV/s. (*E*) Charge–discharge curves of an LSG–MnO_2 (3 min) supercapacitor at different current densities. (*F*) Change of stack capacitance of an LSG–MnO_2 (120 min) supercapacitor as a function of current density. Data for CCG–MnO_2 (120 min) and Au–MnO_2 (120 min) supercapacitors are presented for comparison. (*G* and *H*) Progression of the real (C′) and imaginary (C″) parts of the stack capacitance of CCG (*G*) and LSG (*H*) as a function of frequency. (*I*) Comparison of the LSG–MnO_2 (120 min) hybrid capacitor with a commercially available activated carbon supercapacitor (2.7 V/10 F), pseudocapacitor (2.6 V/35 mF), and a lithium-ion hybrid capacitor (2.3 V/220 F).

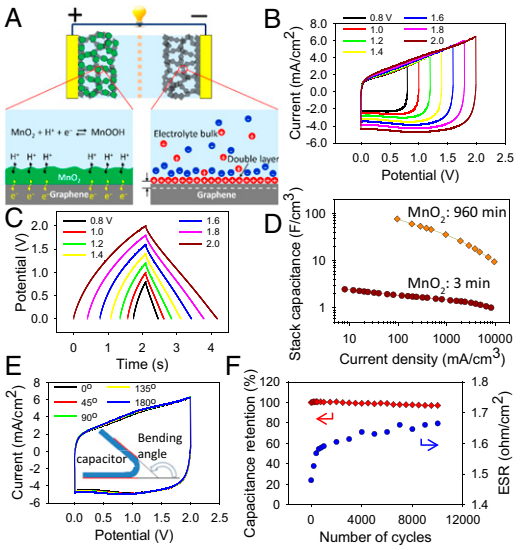

Fig. 5. Asymmetric supercapacitor based on graphene–MnO_2 as the positive electrode and LSG as the negative electrode. (*A*) Schematic showing the structure of the assembled supercapacitor in 1.0 M Na_2SO_4 electrolyte. (*B* and *C*) Electrochemical performance of the asymmetric supercapacitor after increasing the potential window from 0.8 to 2.0 V. (*D*) Change of the stack capacitance as a function of current density. (*E*) Electrochemical performance of the device under different bending angles. (*F*) Cycling stability of the device tested over 10,000 cycles at a scan rate of 1,000 mV/s. Change of the ESR during cycling is also shown.

mesoporous carbon/MnO_2, and 90 F/cm^3 for ultraporous carbon–MnO_2. In addition, depending on the deposition time, ultrahigh areal capacitances of up to ~0.8 F/cm^2 per footprint of the device can be achieved. This compares favorably with commercial carbon supercapacitors that typically provide ~0.3 F/cm^2.

This unprecedented performance can be understood by separating the contribution of the MnO_2 nanoflowers from the average capacitance of the LSG–MnO_2 electrodes. The specific capacitance of MnO_2 depends on the mass of the active material reaching a maximum value of 1145 F/g, which is about 83% of the theoretical capacitance at a mass loading of 13% of MnO_2; Fig. 4*D*. This remarkable performance can be attributed to the electrode microstructure that facilitates the transport of ions and electrons and provides abundant surfaces for charge–transfer reactions, ensuring a greater utilization of the active materials.

To demonstrate the superior properties of LSG–MnO_2 macroporous electrodes, MnO_2 was also electrodeposited on both CCG and gold substrates under the same conditions and their electrochemical performance is presented in Fig. 4*F*. Not only does the CCG–MnO_2 exhibit lower capacitance, but its performance falls off very quickly at higher charge–discharge rates. This can be attributed to the restacking of graphene sheets during the fabrication of the CCG electrodes, resulting in a significant reduction in the surface area and eventually closing off much of the porosity (28). In addition, the Au–MnO_2 supercapacitor shows extremely low capacitance because of the limited surface area and structural properties as can be seen in Fig. 1*A*. LSG–MnO_2, on the other hand, shows a stack capacitance of ~50 F/cm^3 that is more than four times higher than CCG–MnO_2 and about three orders of magnitude higher than Au–MnO_2. The enhanced capacitance and rate capability of the LSG–MnO_2 further confirms its optimized structure, which synergizes the effects of both effective ion migration and high electroactive surface area, thus enabling high and reversible capacitive behavior even at high charge–discharge rates. The optimized ionic diffusion of the LSG network was also confirmed from electrochemical impedance spectroscopy with a response time of 23 ms for LSG compared with 5,952 ms for the CCG electrodes; Fig. 4 *G* and *H*) (see also *SI Appendix*, section 2 and Figs. S1 and S2). In fact, the LSG–MnO_2 supercapacitor shows superior volumetric capacitance and rate capability compared with commercially

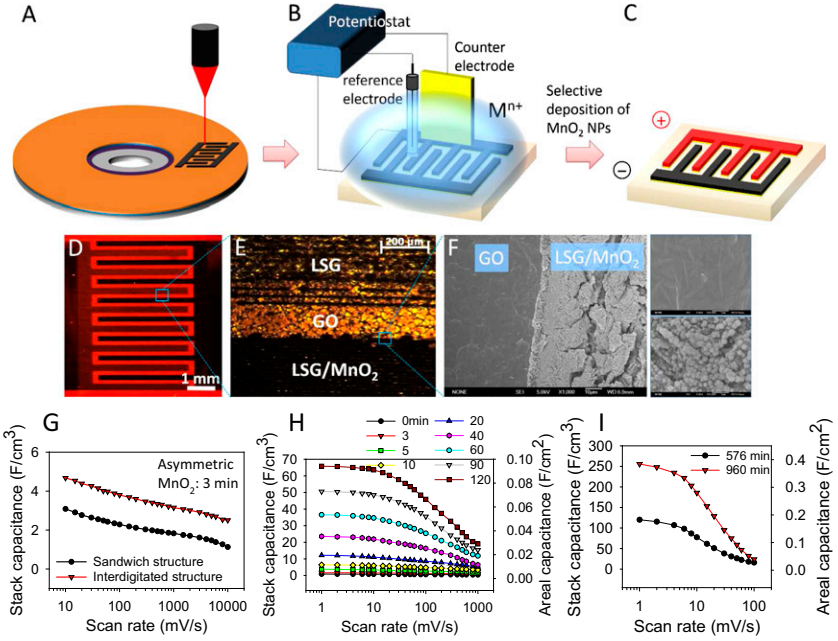

Fig. 6. Engineering of 3D interdigitated microsupercapacitors with high energy density. (*A–C*) Illustration of the fabrication process for an asymmetric microsupercapacitor based on LSG–MnO_2 as the positive electrode and LSG as the negative electrode. (*D*) Photograph showing the asymmetric microsupercapacitor. (*E*) Optical microscope image showing the LSG–GO–LSG-MnO_2 interface. (*F*) SEM image of the interface between GO and LSG shows the selective electrodeposition of MnO_2 on LSG only. (*Inset*) Magnified view of the GO and LSG area. (*G–I*) Comparison of the stack capacitance of the supercapacitor between the sandwich structure and the planar interdigitated structure for (*G*) asymmetric, MnO_2 deposition time 3 min and (*H* and *I*) symmetric devices.

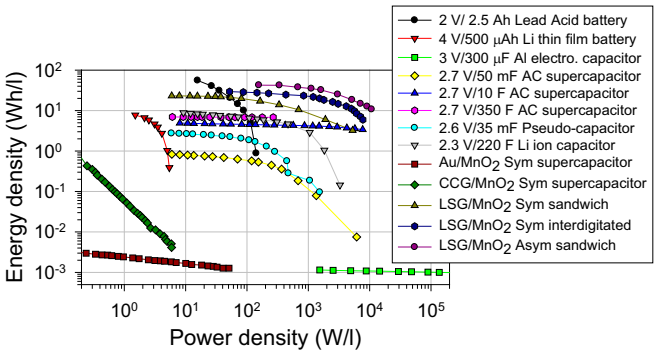

Fig. 7. Ragone plot comparing the energy and power density of LSG–MnO_2 supercapacitors with a number of commercially available energy storage devices: a lead acid battery, a lithium thin-film battery, an aluminum electrolytic capacitor, activated carbon supercapacitors of variable sizes, a pseudocapacitor, and a lithium-ion hybrid capacitor. Performance data for Au–MnO_2 and CCG–MnO_2 are also included to demonstrate the importance of the microstructure of the electrodes.

available activated carbon supercapacitors, pseudocapacitors, and lithium-ion hybrid capacitors as can be seen from Fig. 4*I*.

Construction of Asymmetric Supercapacitors. Considering the high pseudocapacitance of the LSG–MnO_2 electrode and the fast charge–discharge of the double-layer capacitance of the LSG electrode, an asymmetric supercapacitor was assembled using LSG–MnO_2 as the positive and LSG as the negative electrode, as schematically illustrated in Fig. 5*A* (see also *SI Appendix*, section 3). Here, a charge balance between the two electrodes was achieved by controlling the deposition time of MnO_2 at the positive electrode and the thickness of the graphene film at the negative electrode. The electrochemical performance of an asymmetric cell that uses LSG–MnO_2 with 13% MnO_2 mass loading (3-min deposition time) for the positive electrode is shown in Fig. 5 *B* and *C*. The cell exhibits an ideal capacitive behavior with nearly rectangular CV profiles and highly triangular charge/discharge curves; Fig. 5 *B* and *C*. The CV profiles retain their rectangular shape without apparent distortions with increasing scan rates up to an ultrahigh rate of 10,000 mV/s, indicating the high rate capability of this asymmetric supercapacitor. Interestingly, the asymmetric cell presents a wide and stable operating potential window up to 2.0 V in aqueous electrolyte that should afford high energy density. Furthermore, as the MnO_2 deposition time is increased from 3 to 960 min, the stack capacitance increases significantly from around 3 to 76 F/cm^3, meaning that the stored energy and power can be greatly improved in the asymmetric structure; Fig. 5*D*. These cells can also retain their high capacity when faster charge and discharge rates are needed. In addition, the as-fabricated supercapacitor is highly flexible and can be folded and twisted without affecting the structural integrity of the device or its electrochemical performance, holding promise as a practical energy storage system for flexible electronics; Fig. 5*E*.

Long cycle life is another important feature for commercially viable supercapacitors. Indeed, the asymmetric supercapacitor is very stable as it maintains over 96% of its original capacity after 10,000 charge–discharge cycles tested at a high scan rate of 1,000 mV/s; Fig. 5*F*. The equivalent series resistance (ESR) of the supercapacitor was monitored during cycling using a Nyquist plot. The device demonstrates a slight increase of ESR in the first 1,000 cycles with only subtle changes over the remaining cycles.

Three-Dimensional Interdigitated Microsupercapacitors. The development of microsupercapacitors with high capacity per footprint area is crucial for the miniaturization of energy storage devices for modern electronic applications (26). Unfortunately, current state-of-the-art systems still suffer from low areal capacity (26): <11.6 mF/cm^2 for carbons (29, 30), <78 mF/cm^2 for conducting polymers (31), and <56.3 for metal oxides (32). We designed new hybrid microsupercapacitors as illustrated in Fig. 6 *A–C*, in which the positive and negative electrodes are separated into a 3D interdigitated structure. This structure was achieved by combining the techniques of "top-down" LightScribe lithography with "bottom-up" selective electrodeposition. First, 3D interdigitated LSG microelectrodes were produced by the direct writing of graphene patterns on GO films using a consumer-grade LightScribe DVD burner. Subsequently, MnO_2 nanoflowers were selectively electrodeposited on one set of the LSG microelectrodes using the cell setup described in the schematic diagram (*Materials and Methods*). The width of the microelectrodes is adjusted to match the charge between the positive and negative poles of the microdevice. Fig. 6*D* shows a digital photograph of an asymmetric microsupercapacitor that consists of alternating positive and negative electrodes. The lighter microelectrodes correspond to bare graphene (negative electrodes), whereas the other side turns darker in color after the electrodeposition of MnO_2 (positive electrodes). The optical microscope image shows a well-defined pattern and sharp boundaries between the microelectrodes; Fig. 6*E*. SEM further confirmed the conformal structure of this asymmetric microsupercapacitor. A magnified view at the interface between GO and graphene shows the selective electrodeposition of MnO_2 on the graphene area only; Fig. 6*F*.

Electrochemical characterization shows that the asymmetric microsupercapacitor provides enhanced volumetric capacitance and rate capability compared with a conventional sandwich-type asymmetric supercapacitor; Fig. 6*G*. Symmetric hybrid microsupercapacitors show a similar behavior (Fig. 6 *H* and *I*), with the areal capacitance approaching 400 mF/cm^2. To the best of our knowledge, this is the highest areal capacitance achieved so far in an interdigitated microsupercapacitor. The stack capacitance significantly improves to ~250 F/cm^3 (volumetric capacitance per electrode is 1,197 F/cm^3), which is much higher than values previously reported for EDLC, pseudo-, and hybrid microsupercapacitors: 1.3 F/cm^3 for carbon onions, 2.35–3.05 F/cm^3 for graphene, 1.08 F/cm^3 for CNT, 3.1 F/cm^3 for graphene–CNT, 180 F/cm^3 (electrode) for carbide-derived carbon, 588 F/cm^3 for polyaniline nanofibers, 317 F/cm^3 (electrode) for vanadium

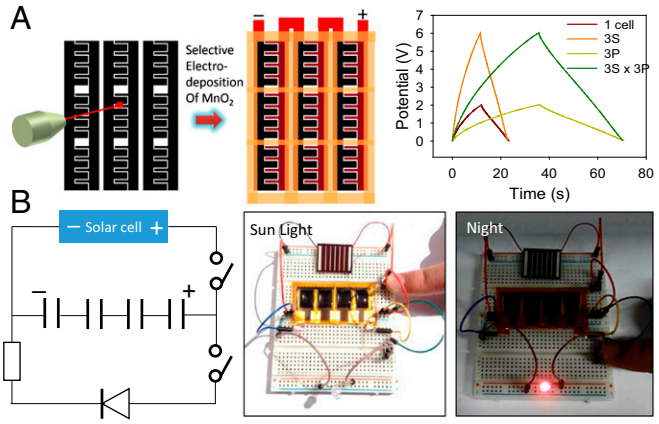

Fig. 8. Direct fabrication of supercapacitor arrays for high-voltage applications and integrated energy storage. (*A*) Direct fabrication of an asymmetric supercapacitor array consisting of 9 cells in a single step. Charge–discharge curves of asymmetric supercapacitor arrays connected in series (3 cells in series, 3S), in parallel (3 cells in parallel, 3P), and in a combination of series and parallel (3 series × 3 parallel, 3S × 3P). A single device is shown for comparison. (*B*) Integration of a supercapacitor array with solar cells for efficient solar energy harvesting and storage.

disulfide nanosheets, and 178 F/cm^3 for molybdenum disulfide nanosheets (*SI Appendix*, Table S2).

Discussion

The energy and power density of the LSG–MnO_2-based supercapacitors are presented in Fig. 7. To put these results in perspective with current technology, we characterized a number of commercially available carbon-based supercapacitors, pseudocapacitors, hybrid supercapacitors, and Li-ion hybrid capacitors and the results are presented in the same plot. These devices were tested under the same dynamic conditions as LSG–MnO_2. For all devices, the calculations were made based on the volume of the full cell that includes the current collector, active material, separator, and electrolyte. The energy density of the hybrid LSG–MnO_2 varies between 22 and 42 Wh/l depending on the configuration (symmetric, asymmetric and sandwich, interdigitated) and the mass loading of MnO_2. By comparison, the LSG–MnO_2 hybrid supercapacitors store about 6 times the capacity of state-of-the-art commercially available EDLC carbon supercapacitors. They are also superior to pseudocapacitors, hybrid supercapacitors, and supercapacitor–lithium-ion battery hybrid (Li-ion capacitors). Furthermore, LSG–MnO_2 supercapacitors can provide power densities up to ∼10 kW/l, which is 100 times faster than high-power lead acid batteries and 1,000 times faster than a lithium thin-film battery.

To meet the high voltage requirements, supercapacitors are often put into a bank of cells connected together in series. This results in bulky supercapacitor modules, which are appropriate in some cases but often cause problems in applications where the total size of the power source is critical. Here, we propose a different design in which an array of separate electrochemical cells is directly fabricated in the same plane and in one step as shown in Fig. 8*A* (see also *SI Appendix*, sections 4, 5 and Figs. S4–S8). This configuration shows very good control over the voltage and current output. In addition, this array can be integrated with solar cells for efficient solar energy harvesting and storage, as shown in Fig. 8*B* and *SI Appendix*, Movie S1.

In summary, we have developed a simple and scalable approach for the fabrication of hybrid LSG–MnO_2 3D supercapacitors and microsupercapacitors that are compact, reliable, and energy dense, charge quickly, and possess long lifetime. Given that MnO_2 is widely used in alkaline batteries [selling ∼10 billion units per year (33)] and the scalability of graphene-based materials, we believe that graphene–MnO_2 hybrid electrodes offer promise for real-world applications.

Materials and Methods

Synthesis of LSG–MnO_2, Au–MnO_2, and CCG–MnO_2 Electrodes. The LSG framework was prepared by focusing a laser beam from a LightScribe DVD burner on a DVD disk coated with graphite oxide. First, the DVD disk is covered by a film of gold-coated polyimide (Astral Technology Unlimited, Inc.) or a sheet of polyethylene terephthalate. This was coated with a 2% GO dispersion in water using the doctor blade technique and left for drying for 5 h under ambient conditions. A computer-designed image is printed onto graphite oxide to make the appropriate LSG pattern (27). This was followed by the electrodeposition of MnO_2 from 0.02 M $Mn(NO_3)_2$ in 0.1 M $NaNO_3$ aqueous solution using a standard three-electrode setup, where a piece of LSG (1 cm^2) is used as the working electrode, Ag–AgCl as the reference electrode (BASi), and a platinum foil (2 cm^2, Sigma-Aldrich) as the counter-electrode. The deposition was achieved by applying a constant current of 250 μA/cm^2 for different time periods between 3 and 960 min. For more information on the assembly of supercapacitors, microsupercapacitors, and characterization methods, please see *SI Appendix, Materials and Methods*.

ACKNOWLEDGMENTS. We thank Matthew Kowal for making graphite oxide dispersions, and Michael Yeung for help with energy dispersive X-ray analysis. This work was supported by Nanotech Energy, Inc.

1. Harrop DP, Zhitomirsky DV (2013) Electrochemical DLC Supercapacitors 2013–2023, Business Report IDTechEx, July 2013. Available at www.idtechex.com. Accessed March, 2015.
2. Simon P, Gogotsi Y (2008) Materials for electrochemical capacitors. *Nat Mater* 7(11): 845–854.
3. Simon P, Gogotsi Y, Dunn B (2014) Materials science. Where do batteries end and supercapacitors begin? *Science* 343(6176):1210–1211.
4. Long JW, et al. (2011) Asymmetric electrochemical capacitors—Stretching the limits of aqueous electrolytes. *MRS Bull* 36(7):513–522.
5. Chen LY, et al. (2013) Toward the theoretical capacitance of RuO_2 reinforced by highly conductive nanoporous gold. *Adv Energy Mater* 3(7):851–856.
6. Xu J, et al. (2013) Flexible asymmetric supercapacitors based upon Co_9S_8 nanorod//Co_3O_4@RuO_2 nanosheet arrays on carbon cloth. *ACS Nano* 7(6):5453–5462.
7. Wang H, et al. (2012) Graphene–nickel cobaltite nanocomposite asymmetrical supercapacitor with commercial level mass loading. *Nano Res* 5(9):605–617.
8. Foo CY, Sumboja A, Tan DJH, Wang J, Lee PS (2014) Flexible and highly scalable V_2O_5-rGO electrodes in an organic electrolyte for supercapacitor devices. *Adv Energy Mater*, 10.1002/aenm.201400236.
9. Ji J, et al. (2013) Nanoporous $Ni(OH)_2$ thin film on 3D ultrathin-graphite foam for asymmetric supercapacitor. *ACS Nano* 7(7):6237–6243.
10. Zhang J, et al. (2011) Asymmetric supercapacitors based on graphene/MnO_2 and activated carbon nanofiber electrodes with high power and energy density. *Adv Funct Mater* 21(12):2366–2375.
11. Bélanger D, Brousse L, Long JW (2008) Manganese oxides: Battery materials make the leap to electrochemical capacitors. *Electrochem Soc Interface* 17(1):49–52.
12. Lang X, Hirata A, Fujita T, Chen M (2011) Nanoporous metal/oxide hybrid electrodes for electrochemical supercapacitors. *Nat Nanotechnol* 6(4):232–236.
13. Su Z, et al. (2014) Scalable fabrication of MnO_2 nanostructure deposited on free-standing Ni nanocone arrays for ultrathin, flexible, high-performance micro-supercapacitor. *Energy Environ Sci* 7(8):2652–2659.
14. Li Q, et al. (2012) Design and synthesis of MnO_2/Mn/MnO_2 sandwich-structured nanotube arrays with high supercapacitive performance for electrochemical energy storage. *Nano Lett* 12(7):3803–3807.
15. Khomenko V, Raymundo-Pinero E, Beguin F (2006) Optimisation of an asymmetric manganese oxide/activated carbon capacitor working at 2 V in aqueous medium. *J Power Sources* 153(1):183–190.
16. Yang P, et al. (2014) Low-cost high-performance solid-state asymmetric supercapacitors based on MnO_2 nanowires and Fe_2O_3 nanotubes. *Nano Lett* 14(2):731–736.
17. Li P, et al. (2014) Core-double-shell, carbon nanotube@polypyrrole@MnO_2 sponge as freestanding, compressible supercapacitor electrode. *ACS Appl Mater Interfaces* 6(7): 5228–5234.
18. Chen W, et al. (2011) High-performance nanostructured supercapacitors on a sponge. *Nano Lett* 11(12):5165–5172.
19. Hu L, et al. (2011) Symmetrical MnO_2-carbon nanotube-textile nanostructures for wearable pseudocapacitors with high mass loading. *ACS Nano* 5(11):8904–8913.
20. Yu G, et al. (2011) Solution-processed graphene/MnO_2 nanostructured textiles for high-performance electrochemical capacitors. *Nano Lett* 11(7):2905–2911.
21. Choi BG, Yang M, Hong WH, Choi JW, Huh YS (2012) 3D macroporous graphene frameworks for supercapacitors with high energy and power densities. *ACS Nano* 6(5):4020–4028.
22. Sumboja A, Foo CY, Wang X, Lee PS (2013) Large areal mass, flexible and free-standing reduced graphene oxide/manganese dioxide paper for asymmetric supercapacitor device. *Adv Mater* 25(20):2809–2815.
23. Zhao X, et al. (2012) Incorporation of manganese dioxide within ultraporous activated graphene for high-performance electrochemical capacitors. *ACS Nano* 6(6): 5404–5412.
24. Zhang Z, et al. (2014) Facile synthesis of 3D MnO2–graphene and carbon nanotube–graphene composite networks for high-performance, flexible, all-solid-state asymmetric supercapacitors. *Adv Energy Mater*, 10.1002/aenm.201400064.
25. Gogotsi Y, Simon P (2011) Materials science. True performance metrics in electrochemical energy storage. *Science* 334(6058):917–918.
26. Beidaghi M, Gogotsi Y (2014) Capacitive energy storage in micro-scale devices: Recent advances in design and fabrication of micro-supercapacitors. *Energy Environ Sci* 7(3):867–884.
27. El-Kady MF, Strong V, Dubin S, Kaner RB (2012) Laser scribing of high-performance and flexible graphene-based electrochemical capacitors. *Science* 335(6074):1326–1330.
28. Yang X, Cheng C, Wang Y, Qiu L, Li D (2013) Liquid-mediated dense integration of graphene materials for compact capacitive energy storage. *Science* 341(6145):534–537.
29. El-Kady MF, Kaner RB (2013) Scalable fabrication of high-power graphene micro-supercapacitors for flexible and on-chip energy storage. *Nat Commun* 4:1475.
30. Pech D, et al. (2010) Ultrahigh-power micrometre-sized supercapacitors based on onion-like carbon. *Nat Nanotechnol* 5(9):651–654.
31. Beidaghi M, Wang C (2011) Micro-supercapacitors based on three dimensional interdigital polypyrrole/C-MEMS electrodes. *Electrochim Acta* 56(25):9508–9514.
32. Wang X, et al. (2013) Manganese oxide micro-supercapacitors with ultra-high areal capacitance. *Nanoscale* 5(10):4119–4122.
33. BAJ Website – Monthly battery sales statistics. Available at web.archive.org/web/20110311224259/www.baj.or.jp/e/statistics/02.php. Accessed October 15, 2014.